Influence of beam collimation on fast-atom diffraction studied via a semiquantum approach

M. S. Gravielle* and J. E. Miraglia
Instituto de Astronomía y Física del Espacio (IAFE, CONICET-UBA), casilla de correo 67, sucursal 28, C1428EGA, Buenos Aires, Argentina
(Received 16 October 2015; published xxxxxx)

The influence of the collimating conditions of the incident beam on diffraction patterns produced by grazing scattering of fast atoms off crystal surfaces is studied within a semiquantum approach, called the surface initial value representation (SIVR) approximation. In this approach we incorporate a realistic description of the incident particle in terms of the collimating parameters, which determine the surface area that is coherently illuminated. The model is applied to He atoms colliding with a LiF(001) surface after passing through a rectangular aperture. As was experimentally observed [Nucl. Instrum. Methods Phys. Res., Sect. B **350**, 99 (2015)], SIVR spectra as a function of the azimuthal angle are very sensitive to the width of the collimating slit. We also found that the length of the collimating aperture affects polar angle distributions, introducing additional interference structures for the longer collimating slits.

DOI: 10.1103/PhysRevA.00.002700 PACS number(s): 34.35.+a, 79.20.Rf, 37.25.+k

I. INTRODUCTION

Diffraction patterns produced by grazing scattering of swift atoms and molecules (with energies in the keV range) on surfaces are nowadays becoming a powerful surface analysis tool, which is giving rise to a technique known as grazing-incidence fast-atom diffraction (GIFAD or FAD) [1,2]. In recent years the FAD method was successfully applied to very different kinds of materials, ranging from insulators [3–5] to semiconductors [6,7] and metals [8–10], as well as structured films [11] and molecules [12] adsorbed on surfaces. However, in spite of the extensive experimental and theoretical work devoted to the research of FAD since its first experimental observation [3,4], the complete understanding of the underlying quantum processes is far from being achieved. In particular, the study of the mechanisms that contribute to the coherence or decoherence of the scattered particles is still in its infancy.

The observation of quantum interference effects for fast atoms impinging on crystal surfaces strongly relies on the preservation of quantum coherence [13–15] and, in this regard, the coherence conditions of the incident beam play an important role. Motivated by Ref. [16], in this article we investigate the influence of the collimation of the incident beam on FAD patterns by making use of a recently developed approach called the surface initial value representation (SIVR) approximation [17]. With this goal we explicitly take into account the experimental collimating conditions to determine the surface region that is *coherently* illuminated by the particle beam and use this information to build the initial wave packet that describes the unperturbed state of the incident particle within the SIVR method.

The SIVR approximation is a semiquantum approach that was derived from the initial value representation (IVR) method by Miller [18] by using the corresponding semiquantum time evolution operator in the frame of a time-dependent distorted-wave formalism. This strategy incorporates an approximate description of classically forbidden transitions on the dark side of rainbow angles, making it possible to avoid the classical rainbow divergence present in previous semiclassical models for FAD, like the surface-eikonal (SE) approach [19,20]. Such a weakness of the SE method affects the intensity of the outermost diffraction maxima when these maxima are close to the classical rainbow angles [10], i.e., the extreme deflection angles of the classical projectile distribution. The SIVR approach, instead, provides an appropriate description of FAD patterns along the whole angular range, even around classical rainbow angles, without requiring the use of convolutions to smooth the theoretical curves [17]. Therefore, the SIVR method can be considered as an attractive alternative to quantum wavepacket propagations, offering a clear representation of the main mechanisms of the process in terms of classical trajectories through the Feynman path integral formulation of quantum mechanics.

In order to analyze the influence of the beam collimation on FAD spectra, an extended version of the SIVR approximation—including the collimating parameters—is applied to evaluate FAD patterns for He atoms grazingly impinging on a LiF(001) surface after going through a rectangular aperture. The paper is organized as follows: The theoretical formalism is summarized in Sec. II. Results for different sizes of the collimating aperture are presented and discussed in Sec. III, while in Sec. IV we outline our conclusions. Atomic units (a.u.) are used unless otherwise stated.

II. THEORETICAL MODEL

Let us consider an atomic projectile P with initial momentum $\vec{K}_i$, which is elastically scattered from a crystal surface S, ending in a final state with momentum $\vec{K}_f$ and total energy $E = K_f^2/(2m_P) = K_i^2/(2m_P)$, with m_P being the projectile mass. By employing the IVR method [21], the scattering state of the projectile at time t can be approximated as [17]

$$\left|\Psi_i^{(\mathrm{SIVR})+}(t)\right\rangle = \frac{1}{(2\pi i)^{3/2}} \int d\vec{R}_o f_i(\vec{R}_o) \int d\vec{K}_o g_i(\vec{K}_o) \times [J_M(t)]^{1/2} \Phi_i(\vec{R}_o) \exp(i S_t) |\vec{\mathcal{R}}_t\rangle, \qquad (1)$$

where

$$\Phi_i(\vec{R}) = (2\pi)^{-3/2} \exp(i \vec{K}_i \cdot \vec{R}) \qquad (2)$$

*Author to whom correspondence should be addressed: msilvia@iafe.uba.ar

is the initial momentum eigenfunction, with $\vec{R}$ being the position of the center of mass of the incident atom, and the sign "+" in the supra-index of the scattering state indicates that it satisfies outgoing asymptotic conditions. In Eq. (1) the position ket $|\vec{\mathcal{R}}_t\rangle$ is associated with the time-evolved position of the incident atom at a given time t, $\vec{\mathcal{R}}_t \equiv \vec{\mathcal{R}}_t(\overrightarrow{R}_o, \overrightarrow{K}_o)$, which is derived by considering a classical trajectory with starting position and momentum $\overrightarrow{R}_o$ and $\overrightarrow{K}_o$, respectively. The function S_t denotes the classical action along the trajectory

$$S_t = S_t(\overrightarrow{R}_o, \overrightarrow{K}_o) = \int_0^t dt' \left[\frac{\overrightarrow{\mathcal{P}}_{t'}^2}{2m_P} - V_{\mathrm{SP}}(\vec{\mathcal{R}}_{t'}) \right], \tag{3}$$

with $\overrightarrow{\mathcal{P}}_t = m_P d\vec{\mathcal{R}}_t/dt$ being the classical projectile momentum at the time t and V_{SP} being the surface-projectile interaction, while the function

$$J_M(t) = \det \left[\frac{\partial \vec{\mathcal{R}}_t(\overrightarrow{R}_o, \overrightarrow{K}_o)}{\partial \overrightarrow{K}_o} \right] \tag{4}$$

is a Jacobian factor (a determinant) evaluated along the classical trajectory $\vec{\mathcal{R}}_t$. This Jacobian factor can be related to the Maslov index [22] by expressing it as $J_M(t) = |J_M(t)| \exp(i\nu_t\pi)$, where $|J_M(t)|$ is the modulus of $J_M(t)$ and ν_t is an integer number that accounts for the sign of $J_M(t)$ at a given time t. In this way, ν_t represents a time-dependent Maslov index, satisfying the condition that, every time that $J_M(t)$ changes its sign along the trajectory, ν_t increases by 1.

The functions $f_i(\overrightarrow{R}_o)$ and $g_i(\overrightarrow{K}_o)$, present in the integrand of Eq. (1), describe the shape of the position and momentum wave packet associated with the incident projectile. In a previous paper [17] $f_i(\overrightarrow{R}_o)$ was considered as a Gaussian distribution illuminating a fixed number of reduced unit cells of the crystal surface, while $g_i(\overrightarrow{K}_o)$ was defined as a uniform distribution. Here these functions are derived from the collimation conditions of the incident beam in order to incorporate a realistic profile of the coherent initial wave packet, as explained in the following section.

By using the SIVR scattering state, given by Eq. (1), within the framework of the time-dependent distorted-wave formalism [23], the SIVR transition amplitude, per unit of surface area $\mathcal{S}$, can be expressed as [17]

$$A_{if}^{(\mathrm{SIVR})} = \frac{1}{\mathcal{S}} \int_{\mathcal{S}} d\overrightarrow{R}_o f_i(\overrightarrow{R}_o) \int d\overrightarrow{K}_o g_i(\overrightarrow{K}_o) \times a_{if}^{(\mathrm{SIVR})}(\overrightarrow{R}_o, \overrightarrow{K}_o), \tag{5}$$

where

$$a_{if}^{(\mathrm{SIVR})}(\overrightarrow{R}_o, \overrightarrow{K}_o) = -\int_0^{+\infty} dt \frac{|J_M(t)|^{1/2} e^{i\nu_t\pi/2}}{(2\pi i)^{9/2}} V_{\mathrm{SP}}(\vec{\mathcal{R}}_t) \times \exp\left[i\left(\varphi_t^{(\mathrm{SIVR})} - \overrightarrow{Q} \cdot \overrightarrow{R}_o\right)\right] \tag{6}$$

is the partial transition amplitude associated with the classical path $\vec{\mathcal{R}}_t \equiv \vec{\mathcal{R}}_t(\overrightarrow{R}_o, \overrightarrow{K}_o)$, with $\overrightarrow{Q} = \vec{K}_f - \vec{K}_i$ being the projectile momentum transfer and

$$\varphi_t^{(\mathrm{SIVR})} = \int_0^t dt' \left[\frac{1}{2m_P} (\vec{K}_f - \overrightarrow{\mathcal{P}}_{t'})^2 - V_{\mathrm{SP}}(\vec{\mathcal{R}}_{t'}) \right] \tag{7}$$

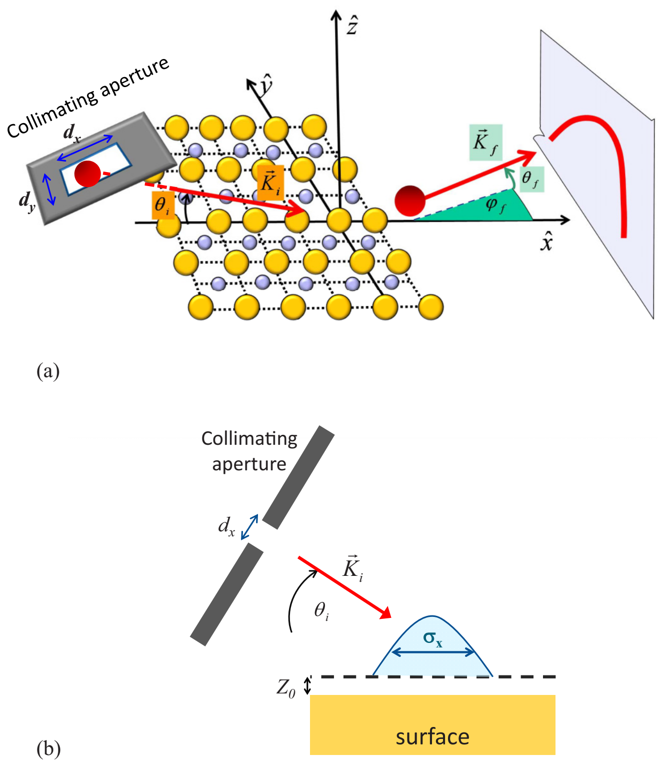

FIG. 1. (Color online) (a) Sketch of the FAD process, including the collimating aperture. (b) Lateral sight of the scattering process.

being the SIVR phase at the time t. Details of the derivation of the SIVR method are given in Ref. [17].

In this article we use a frame of reference placed on the first atomic layer, with the surface contained in the x-y plane, the $\widehat{x}$ versor along the incidence direction and the $\widehat{z}$ versor oriented perpendicular to the surface, aiming towards the vacuum region. The SIVR differential probability, per unit of surface area, for elastic scattering with final momentum $\vec{K}_f$ in the direction of the solid angle $\Omega_f \equiv (\theta_f, \varphi_f)$, is obtained from Eq. (5) as

$$dP^{(\mathrm{SIVR})}/d\Omega_f = K_f^2 \left| A_{if}^{(\mathrm{SIVR})} \right|^2, \tag{8}$$

where θ_f and φ_f are the final polar and azimuthal angles, respectively, with θ_f measured with respect to the surface and φ_f measured with respect to the $\widehat{x}$ axis. A schematic depiction of the process and the coordinates is displayed in Fig. 1(a).

Size of initial *coherent* wave packet

In Eq. (5), the variables $\overrightarrow{R}_o$ and $\overrightarrow{K}_o$ represent the starting position and momentum, respectively, of the classical projectile trajectory, both measured at $t = 0$, while the functions $f_i(\overrightarrow{R}_o)$ and $g_i(\overrightarrow{K}_o)$ determine the shape of the initial wave packet, satisfying the Heisenberg uncertainty relation. We decompose the starting position as $\overrightarrow{R}_o = \overrightarrow{R}_{os} + Z_o\widehat{z}$, where $\overrightarrow{R}_{os} = X_o\widehat{x} + Y_o\widehat{y}$ and Z_o are the components parallel and perpendicular, respectively, to the surface plane, with Z_o being a fixed distance for which the projectile is hardly affected by the surface interaction.

We assume that the size of the coherent initial wave packet, at a distance Z_o from the surface, is governed by the collimation of the incident beam as given by the Van Cittert–Zernike theorem [24]. By considering a rectangular collimating aperture placed a long distance L from the surface, the coherence size of the incident beam on the Z_o plane, which is located parallel to the surface at a distance Z_o from it, is defined by the complex grade of coherence, $\mu(X_o,Y_o)$. It reads [24]

$$|\mu(X_o,Y_o)|^2 = j_0^2\left(\frac{\pi d_x}{\lambda_\perp L'}X_o\right)j_0^2\left(\frac{\pi d_y}{\lambda L'}Y_o\right), \tag{9}$$

where $j_0(x)$ is the spherical Bessel function and d_x and d_y denote the lengths of the sides of the rectangular aperture, which form angles $\theta_x = \pi/2 - \theta_i$ and $\theta_y = 0$, respectively, with the surface plane, and θ_i being the glancing incidence angle [see Figs. 1(a) and 1(b)]. In Eq. (9) the de Broglie wavelengths λ and $\lambda_\perp$ are defined as

$$\lambda = 2\pi/K_i \quad \text{and} \quad \lambda_\perp = \lambda/\sin\theta_i, \tag{10}$$

respectively, this last one being associated with the initial motion normal to the surface plane, while $L' = L - Z_o/\sin\theta_i$. For most of the collision systems, Z_o can be chosen as equal to the lattice constant of the crystal, leading to $L' \cong L$.

According Eq. (9) the spatial profile of the initial wave packet can be approximated by a product of Gaussian functions,

$$G(\omega,x) = [2/(\pi\omega^2)]^{1/4}\exp(-x^2/\omega^2), \tag{11}$$

as follows:

$$f_i(\vec{R}_{os}) = G(\sigma_x,X_o)G(\sigma_y,Y_o), \tag{12}$$

where the parameters σ_x and σ_y were derived by fitting the complex grade of coherence, i.e., $|\mu(X_o,Y_o)|^2 \simeq |f_i(\vec{R}_{os})|^2$, reading

$$\sigma_x = \frac{\lambda_\perp}{\sqrt{2}}\frac{L}{d_x}, \quad \sigma_y = \frac{\lambda}{\sqrt{2}}\frac{L}{d_y}. \tag{13}$$

The lengths σ_x and σ_y represent the effective widths of the $|G(\sigma_x,X_o)|^2$ and $|G(\sigma_y,Y_o)|^2$ distributions, respectively, being defined as the corresponding root-mean-square deviations [25]. Notice that these widths are associated with the *transversal coherence size* of the initial wave packet, a magnitude that is crucial in matter-wave interferometry [26–28].

On the other hand, concerning the momentum profile of the initial wave packet, as we are dealing with an incident beam with a well-defined energy, i.e., $\Delta E/E \ll 1$ [16], the *longitudinal coherence length* does not play any role [26]. Consequently, the starting momentum $\vec{K}_o$ satisfies energy conservation, with $K_0 = |\vec{K}_0| = \sqrt{2m_P E}$, and the integration on $\vec{K}_0$ can be solved by making use of the change of variables $\vec{K}_o = K_o(\cos\theta_o\cos\varphi_o, \cos\theta_o\sin\varphi_o, -\sin\theta_o)$, with θ_o and φ_o varying around the incidence angles θ_i and $\varphi_i = 0$, respectively. The shape of the corresponding angular wave packet is described again in terms of Gaussian functions, reading

$$g_i(\vec{K}_o) \simeq g_i(\Omega_o) = G(\sigma_\theta,\theta_o - \theta_i)G(\sigma_\varphi,\varphi_o), \tag{14}$$

where $\Omega_o \equiv (\theta_o,\varphi_o)$ is the solid angle corresponding to the $\vec{K}_o$ direction and the angular widths of the θ_o and φ_o distributions were derived from the uncertainty principle as [25]

$$\sigma_\theta = \frac{\lambda_\perp}{2\sigma_x} \quad \text{and} \quad \sigma_\varphi = \frac{\lambda}{2\sigma_y}, \tag{15}$$

respectively.

Replacing Eqs. (12) and (14) in Eq. (5), the extended version of the SIVR transition amplitude, including explicitly the proper shape of the incident wave packet, is expressed as

$$A_{if}^{(\mathrm{SIVR})} = \frac{\alpha}{S}\int_S d\vec{R}_{os}\, f_i(\vec{R}_{os})\int d\Omega_o\, g_i(\Omega_o)\, a_{if}^{(\mathrm{SIVR})}(\vec{R}_o,\vec{K}_o), \tag{16}$$

where $a_{if}^{(\mathrm{SIVR})}(\vec{R}_o,\vec{K}_o)$ is given by Eq. (6) and $\alpha = m_P K_i$.

III. RESULTS

We apply the extended SIVR method to ^{4}He atoms elastically scattered from a LiF(001) surface under axial surface channeling conditions since, for this collision system, diffraction patterns for different widths of the collimating slit were reported in Ref. [16]. The SIVR transition amplitude was obtained from Eq. (16) by employing the Monte Carlo technique to evaluate the $\vec{R}_{os}$ and Ω_o integrals, considering more than 4×10^5 points in such an integration. For every starting point, the partial transition amplitude $a_{if}^{(\mathrm{SIVR})}(\vec{R}_o,\vec{K}_o)$ was evaluated numerically from Eq. (6) by employing a potential V_{SP} derived from a pairwise additive hypothesis. The potential model used in this work is the same as the one employed in Ref. [17]. It describes the surface-projectile interaction as the sum of the static and polarization contributions, the first of them evaluated incorporating no local terms of the electronic density in the kinetic and exchange potentials. The potential V_{SP} also takes into account a surface rumpling, with a displacement distance extracted from Ref. [20]. Details of the surface potential will be published elsewhere [29].

In this work we vary the size of the collimating aperture, keeping a fixed incidence condition given by helium projectiles impinging along the $\langle 110\rangle$ channel with a total energy $E =$ 1 keV and an incidence angle $\theta_i = 0.99^\circ$. In all the cases, the distance between the collimating aperture and the surface is chosen as $L = 25$ cm, in agreement with the experimental setup of Ref. [16].

In Figs. 2 and 3 we show two-dimensional projectile distributions, as a function of θ_f and φ_f, derived within the SIVR approximation by considering collimation slits with the same length—$d_x = 1.5$ mm—but two different widths: $d_y = 0.2$ mm and $d_y = 1.0$ mm, respectively. Both SIVR distributions reproduce quite well the corresponding experimental distributions [16], which are also displayed in the figures. They present the usual banana shape, characteristic of the axial surface scattering [30], with final dispersion angles lying on a thick annulus, whose mean radius is approximately equal to θ_i. From the comparison of Figs. 2 and 3 it is clearly observed that the width of the collimation slit strongly affects the diffraction patterns, making the well-defined peaks present in the distributions of Fig. 2, for the more narrow slit, completely disappear when the width of the slit is increased,

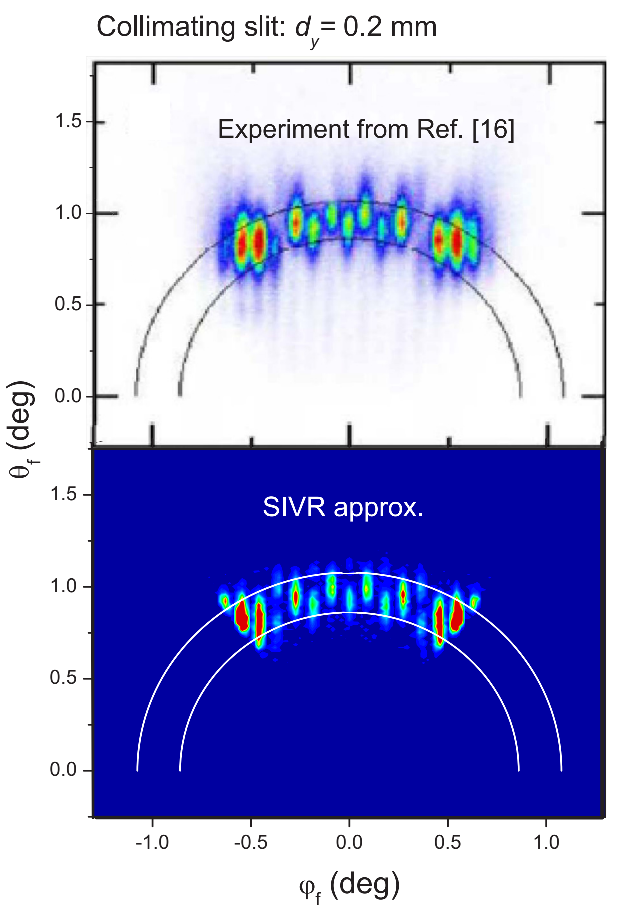

FIG. 2. (Color online) Two-dimensional projectile distribution as a function of the final dispersion angles θ_f and φ_f, for 1 keV ^{4}He atoms impinging on LiF(001) along the $\langle 110\rangle$ direction with the incidence angle $\theta_i = 0.99^{\circ}$. The incident helium beam is collimated with a rectangular aperture of sides $d_x = 1.5$ mm and $d_y = 0.2$ mm. Upper panel shows experimental distribution extracted from Ref. [16]; lower panel shows SIVR distribution.

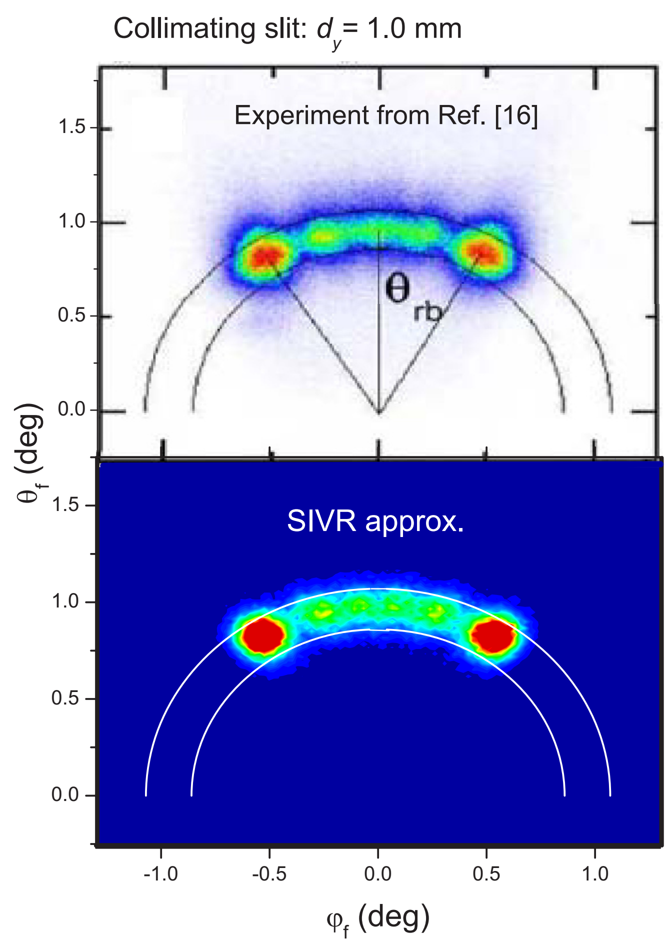

FIG. 3. (Color online) Similar to Fig. 2 for a collimating aperture of sides $d_x = 1.5$ mm and $d_y = 1.0$ mm. The radial lines in the upper panel indicate the positions of the rainbow deflection angles $\pm\Theta_{rb}$.

as happens in Fig. 3. In the experimental and theoretical intensity distributions of Fig. 3, only the maxima at the rainbow deflection angles $\pm\Theta_{rb}$ are visible. As discussed in Ref. [16], this behavior is related to the area $\mathcal{S}$ of the surface plane that is coherently lighted by the incident beam and will be studied in detail within the SIVR approach.

In Eq. (16), by splitting the $\overrightarrow{R}_{os}$ integral over the area $\mathcal{S}$ into a collection of integrals over different reduced unit cells, it is possible to express $A_{if}^{(\mathrm{SIVR})}$ as a product of two factors [17]:

$$A_{if}^{(\mathrm{SIVR})} \simeq A_{if,1}^{(\mathrm{SIVR})} F_B, \qquad (17)$$

each of them associated with a different interference mechanism. The factor $A_{if,1}^{(\mathrm{SIVR})}$, called a unit-cell form factor, is derived from Eq. (16) by evaluating the $\overrightarrow{R}_{os}$ integral over only one reduced unit cell, being related to supernumerary rainbows [31]. While the factor F_B is a crystallographic factor associated with Bragg diffraction, which originates from the interference of identical trajectories whose initial positions $\overrightarrow{R}_{os}$ are separated by a distance equal to the spatial periodicity of the lattice. The factor F_B depends on $\overrightarrow{Q}$ and the area $\mathcal{S}$ coherently illuminated by the particle beam, being insensible to the potential model.

In Eq. (16) the effective area $\mathcal{S}$ coherently lighted by the incident beam can be estimated as $\mathcal{S} \simeq \mathcal{D}_x\mathcal{D}_y$, where the distances $\mathcal{D}_j = 2\sqrt{2}\sigma_j$ with $j = x,y$ were determined from the (X_o,Y_o) values for which the function $|\mu(X_o,Y_o)|^2$, given by Eq. (9), vanishes. Under typical incidence conditions for FAD, the dependence of F_B on the azimuthal angle φ_f becomes completely governed by the number n_y of reduced unit cells in the direction transversal to the incidence channel that are coherently illuminated by the initial wave packet, i.e., $n_y \simeq \mathcal{D}_y/a_y$, where a_y is the length of the reduced unit cell along the $\widehat{y}$ direction. For $n_y \gtrsim 2$ the factor F_B gives rise to Bragg peaks placed at azimuthal angles that verify the relation $\sin\varphi_f = m\lambda/a_y$, with m being an integer, as observed in Fig. 2 where $n_y \simeq 4$. The relative intensities of theses Bragg peaks are modulated by $A_{if,1}^{(\mathrm{SIVR})}$, which acts as an envelope function that can reduce or even suppress the contribution of a given Bragg order, while the peak width is determined by n_y, narrowing as n_y increases. But when the coherently illuminated region shrinks to cover around a reduced unit cell in the transversal direction, only the unit-cell factor is present

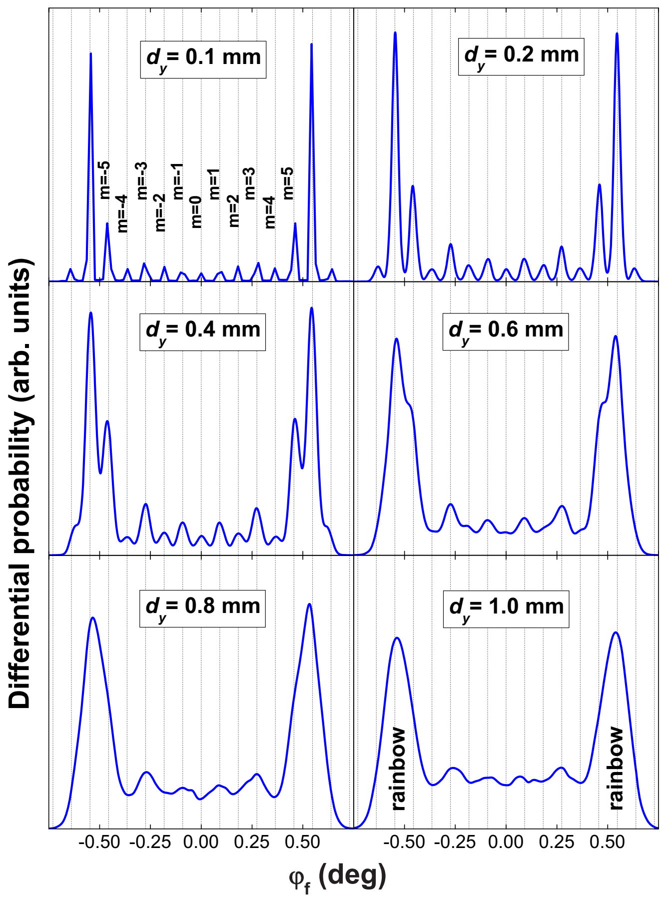

FIG. 4. (Color online) Azimuthal angular distribution as a function of φ_f for 1 keV ^{4}He atoms impinging on LiF(001) along the $\langle 110\rangle$ direction with the incidence angle $\theta_i = 0.99°$. The incident helium beam is collimated with a rectangular aperture of length $d_x = 1.5$ mm and different widths: $d_y = 0.1, 0.2, 0.4, 0.6, 0.8$, and 1.0 mm, respectively. Vertical lines indicate the angular positions of Bragg peaks, as explained in the text.

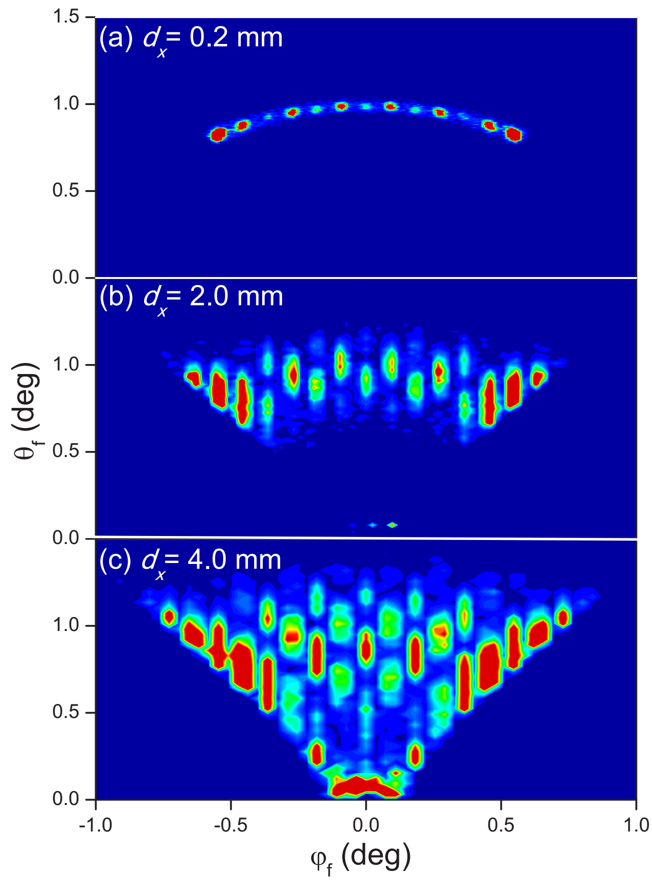

FIG. 5. (Color online) Similar to Fig. 2 for a collimating slit of width $d_y = 0.2$ mm and different lengths: (a) $d_x = 0.2$ mm, (b) $d_x = 2.0$ mm, and (c) $d_x = 4.0$ mm.

in Eq. (17). Consequently, the angular distribution shows structures associated with supernumerary rainbow maxima exclusively, as it happens in Fig. 3 where $n_y \lesssim 1$.

With the aim of studying more deeply the variation of the diffraction patterns with the width of the slit, in Fig. 4 we display the differential probability $dP^{(\mathrm{SIVR})}/d\varphi_f$, as a function of the azimuthal angle φ_f, for different values of d_y. As given by Eq. (13), when d_y augments, the number n_y of the coherently illuminated cells decreases while the width of the Bragg peaks increases, as observed in Fig. 4 for $d_y \lesssim 0.4$ mm. For wider collimating slits Bragg peaks start to blur out, disappearing completely for $d_y = 0.8$ mm, where $n_y \simeq 1$. Therefore, varying d_y we can inspect two different zoologies: Bragg peaks at small d_y values and supernumerary rainbow peaks at large d_y.

We also investigate the influence of the length of the collimating aperture, d_x, on FAD patterns. In Fig. 5 we display angular projectile distributions derived from the SIVR approach by considering a collimating slit with the same width, $d_y = 0.2$ mm, and three different lengths: $d_x = 0.2$, 2.0, and 4.0 mm. For a small square aperture [Fig. 5(a)], Bragg peaks are observed like circular spots lying on a thin ring whose radius is equal to θ_i, corresponding to an almost ideal elastic rebound $\vec{K}_i \to \vec{K}_f$. But when the length of the collimating aperture augments up to $d_x = 2.0$ mm [Fig. 5(b)], transforming the square orifice into a slit, Bragg peaks become visible like elongated strips which are placed at slightly different radius. This effect is even more evident in Fig. 5(c) for $d_x = 4.0$ mm, where the projectile distribution resembles the diffraction charts for different normal energies $E_\perp = E \sin^2 \theta_i$. The explanation is simple: from Eqs. (13) and (15), if d_x is large σ_θ is also large, enabling a wide spread of the impact momentum normal to the surface plane, $|K_{oz}| = K_o \sin\theta_o$. Such a K_{oz} dispersion gives rise to the structures along the vertical axis of Fig. 5(c). Hence, the intensity oscillations along the θ_f axis observed for long collimating slits are probing the surface potential for different distances to the topmost atomic plane. They might be a useful tool to explore different distances to the surface without varying the mean value of the normal energy $E_\perp$.

The previous analysis was done by keeping the de Broglie wavelengths of Eq. (10) constant. However, the size of the coherently illuminated region is affected by the λ and $\lambda_\perp$ values, as given by Eq. (13). Then, in FAD experiments, the dimensions of the collimating aperture should be modified for every incidence condition in order to ensure a similar coherent lighting of the surface in all cases. Additionally, notice that the transversal coherence length σ_x (σ_y) depends on the ratio L/d_x (L/d_y), so that any change of the collimating conditions that keeps this ratio constant would produce the same interference patterns. Furthermore, even though the present results were obtained by considering rectangular collimating apertures, the main outcomes of the work are expected to hold also for circular collimating apertures.

IV. CONCLUSIONS

We derived an extended version of the SIVR approximation [17] that incorporates a realistic description of the coherent initial wave function in terms of the collimating parameters of the incident beam. The model was applied to helium atoms impinging at grazing angles on a LiF(001) surface considering a rectangular collimating aperture with different sizes. As was found experimentally [16], the SIVR interference patterns are strongly affected by the width of the collimating slit, which determines the transversal length of the surface area that is coherently illuminated by the incident wake packet. The number of lighted reduced unit cells in the direction transverse to the incidence channel determines the azimuthal width of the Bragg peaks, making either Bragg peaks or supernumerary rainbows visible. Therefore, knowledge of the experimental collimating conditions is essential for a meaningful comparison with theoretical distributions.

On the other hand, the length of the collimating slit affects the polar θ_f distribution of scattered projectiles, this effect being related to the dispersion of the component of the initial momentum perpendicular to the surface. As the length of the collimating aperture increases, diffraction maxima are transformed from circular spots into elongated strips, where interference structures along the θ_f axis arise for the longer slits. These findings suggest that collimating slits with several millimeters of length might be used to probe the projectile-surface interaction for different normal distances. Alternatively, if the usual diffraction charts are employed for surface analysis, sufficiently short collimating apertures are required to ensure a small dispersion of the initial perpendicular energy.

ACKNOWLEDGMENTS

The authors acknowledge financial support from CONICET, UBA, and ANPCyT of Argentina.

[1] H. Winter and A. Schüller, Prog. Surf. Sci. **86**, 169 (2011), and references therein.

[2] A. Zugarramurdi *et al.*, Appl. Phys. Lett. **106**, 101902 (2015).

[3] A. Schüller, S. Wethekam, and H. Winter, Phys. Rev. Lett. **98**, 016103 (2007).

[4] P. Rousseau, H. Khemliche, A. G. Borisov, and P. Roncin, Phys. Rev. Lett. **98**, 016104 (2007).

[5] A. Schüller *et al.*, Surf. Sci. **606**, 161 (2012).

[6] H. Khemliche, P. Rousseau, P. Roncin, V. H. Etgens, and F. Finocchi, Appl. Phys. Lett. **95**, 151901 (2009).

[7] M. Debiossac, A. Zugarramurdi, H. Khemliche, P. Roncin, A. G. Borisov, A. Momeni, P. Atkinson, M. Eddrief, F. Finocchi, and V. H. Etgens, Phys. Rev. B **90**, 155308 (2014).

[8] N. Bundaleski, H. Khemliche, P. Soulisse, and P. Roncin, Phys. Rev. Lett. **101**, 177601 (2008).

[9] M. Busch, A. Schüller, S. Wethekam, and H. Winter, Surf. Sci. **603**, L23 (2009).

[10] C. A. Ríos Rubiano, G. A. Bocan, M. S. Gravielle, N. Bundaleski, H. Khemliche, and P. Roncin, Phys. Rev. A **87**, 012903 (2013).

[11] J. Seifert, A. Schüller, H. Winter, R. Wlodarczyk, J. Sauer, and M. Sierka, Phys. Rev. B **82**, 035436 (2010).

[12] J. Seifert, M. Busch, E. Meyer, and H. Winter, Phys. Rev. Lett. **111**, 137601 (2013).

[13] F. Aigner, N. Simonović, B. Solleder, L. Wirtz, and J. Burgdörfer, Phys. Rev. Lett. **101**, 253201 (2008).

[14] J. Lienemann *et al.*, Phys. Rev. Lett. **106**, 067602 (2011).

[15] N. Bundaleski, P. Soulisse, A. Momeni, H. Khemliche, and P. Roncin, Nucl. Instrum. Methods Phys. Res., Sect. B **269**, 1216 (2011).

[16] J. Seifert, J. Lienemann, A. Schüller, and H. Winter, Nucl. Instrum. Methods Phys. Res., Sect. B **350**, 99 (2015).

[17] M. S. Gravielle and J. E. Miraglia, Phys. Rev. A **90**, 052718 (2014).

[18] W. H. Miller, J. Chem. Phys. **53**, 3578 (1970).

[19] M. S. Gravielle and J. E. Miraglia, Phys. Rev. A **78**, 022901 (2008).

[20] A. Schüller, H. Winter, M. S. Gravielle, J. M. Pruneda, and J. E. Miraglia, Phys. Rev. A **80**, 062903 (2009).

[21] W. H. Miller, J. Phys. Chem. A **105**, 2942 (2001).

[22] R. Guantes, A. S. Sanz, J. Margalef-Roig, and S. Miret-Artés, Surf. Sci. Rep. **53**, 199 (2004).

[23] D. P. Dewangan and J. Eichler, Phys. Rep. **247**, 59 (1994).

[24] M. Born and E. Wolf, *Principles of Optics* (Pergamon Press, Oxford, 1986), Chap. 10.

[25] C. Cohen-Tannoudji, B. Diu, and F. Laloë, *Quantum Mechanics* (Willey-VCH, Paris, 2011).

[26] A. Tonomura, *Progress in Optics 23* (North-Holland, Amsterdam, 1986), p. 183.

[27] C. Keller, J. Schmiedmayer, and A. Zeilinger, Opt. Commun. **179**, 129 (2000).

[28] I. Fabre, F. Navarrete, L. Sarkadi, and R. O. Barrachina, J. Phys.: Conf. Ser. **635**, 042003 (2015).

[29] J. E. Miraglia and M. S. Gravielle (unpublished).

[30] F. W. Meyer, L. Folkerts, and S. Schippers, Nucl. Instrum. Methods Phys. Res., Sect. B **100**, 366 (1995).

[31] A. Schüller and H. Winter, Phys. Rev. Lett. **100**, 097602 (2008).